Food Control 192 (2027) 112581

Contents lists available at ScienceDirect

Food Control

journal homepage: www.elsevier.com/locate/foodcont

Acrylamide prediction on chestnut-based biscuits, a shaped matter

Alessandro Zanchin [a,*], Marco Napoli [b], Antonio Pescatore [b], Nicolò Cecchin [a], Lorenzo Guerrini [a]

[a] Department of Land, Environment, Agriculture and Forestry, University of Padua, Legnaro, 35020, Italy
[b] Department of Agriculture, Food, Environment and Forestry, University of Florence, Florence, 50144, Italy

ARTICLE INFO

Keywords:
Hyperspectral imaging
3D analysis
Morphology
Thermal camera
Colour analysis
Bakery foods

ABSTRACT

The detection and removal of contaminants through non-contact sensors remain challenging in bakery products. The chemical composition and the brown colour of goods made with alternative flours, such as chestnut-flour-based dough, may compromise the sensitivity of colour and hyperspectral analysis, which are widely acknowledged non-contact techniques for acrylamide detection in heated goods. Furthermore, empirical models proposed in the literature often neglect the effect of product shape and its relationship with acrylamide formation.

In the present study, chestnut flour-based biscuits were shaped into four shapes and baked at incremental times. Colour, hyperspectral, and thermal analyses of the biscuit surface were correlated with acrylamide content, measured by an ELISA-based method. In addition, a morphological evaluation was performed using three-dimensional photogrammetry, enabling the extraction of shape descriptors relevant to the biscuit's surface warming dynamics.

Acrylamide content was predicted using features derived from these datasets. Colour analysis outperformed the other feature types. Lightness and the blue-yellow component yielded more meaningful results than the green-red component. Among the different biscuit shapes, the measured surface area and surface roughness emerged as relevant factors for adjusting acrylamide content in each biscuit, highlighting the importance of morphology in predictive modelling.

Finally, the best prediction model could estimate acrylamide content across the investigated baking conditions, with an average prediction error of 44.59 μg kg^{-1}, by combining two colour-derived predictors with two morphological descriptors.

1. Introduction

Since its discovery in food in 2002, 2-propenamide, hereafter referred to as acrylamide (AA), has received considerable attention. In fact, AA had already been classified by the International Agency for Research on Cancer (IARC) as probably carcinogenic to humans (Group 2A) (IARC, 1994). AA is mainly formed in oven-cooked, fried vegetables, roasted coffee, and cereal-based products (Keramat et al., 2011).

Although no strict regulatory limits are imposed, the European Union has defined benchmark levels for different food categories, including 350 μg kg^{-1} for biscuits and wafers and 50 μg kg^{-1} for wheat-based bread (European Commission, 2017). No more limitations are available from the U.S. or other countries. Heat is the main driver of AA synthesis. Heat transfer depends on cooking temperature and on the contribution of conduction, radiation, convection, or their combinations, depending on the cooking system. In bakery products, baking promotes dough warming, with a greater effect at the external surface, which is directly exposed to the heat sources. In the surface layers of baked products, water evaporation is more intense than in the deeper layers, where retained water diffuses slowly toward the surface. Consequently, water content (WC) can differ by approximately 2% between the crust and a layer 2 mm below the surface in baked bread (Ahrne et al., 2007). The lower WC at the surface allows the surface temperature to rise above 100 °C, while the core temperature generally does not exceed 100 °C due to the higher WC. As a result, crust temperature tends to approach the oven air temperature. In these conditions, the Maillard reaction can proceed while the temperature continues to increase. Temperatures above 120 °C are widely recognised as the minimum required for AA formation (Contaminants in the Food Chain, 2015). Free asparagine (fAsn) and reducing sugars (Sug) are

* Corresponding author.
E-mail address: alessandro.zanchin@unipd.it (A. Zanchin).

https://doi.org/10.1016/j.foodcont.2026.112581
Received 9 April 2026; Received in revised form 19 August 2026; Accepted 24 August 2026
Available online 27 August 2026

the main reactants involved in AA synthesis. At very high temperatures (approximately 180 °C), AA degradation may also occur, producing degradation products (Deg), as outlined in Eq. (1) (Claeys et al., 2005). Consequently, AA concentration can be approximated by a pseudo-first-order kinetic model, while degradation kinetics are not always predictable (Açar & Gökmen, 2010).

$$\text{fAsn} + \text{Sug} \overset{k_s}{\rightarrow} AA \overset{k_d}{\rightarrow} Deg \tag{1}$$

The AA synthesis rate (k_s) and the AA degradation rate (k_d) depend primarily on baking temperature and the activation energy. Activation energy is ingredient-dependent (Jensen et al., 2025; Van Der Fels-Klerx et al., 2014), whereas baking temperature provides the energy required to activate the reaction pathways (Claeys et al., 2005). As a result, AA predominantly accumulates in the crust of bakery products, with only trace amounts detected in the inner crumb. This spatial heterogeneity leads to the so-called "crust model" (Gökmen & Açar, 2009). Under this framework, food thickness and surface-to-volume ratio (SA:V) are relevant for predicting AA accumulation and optimising baking conditions (Manley & Clark, 2011).

The highest AA content is observed in fried chips and roasted coffee, both of which are attributed to the matrix composition and heating process, followed by baked goods. More in detail, coffee contains the highest sucrose concentration (on average 73 mg g^{-1} drymass) (Murkovic & Derler, 2006), while potatoes contain the highest fAsn concentration (ranging within 9–14 mg g^{-1} drymass) (Muttucumaru et al., 2015). Sucrose and fAsn content in common wheat flours was established around 3.5 and 1.5 mg g^{-1} drymass, respectively (Žilić et al., 2017). Secondly, at 180 °C, the different heating methods favour convective heat transfer coefficients in deep frying (estimated at 247–275 W m^{-2} K^{-1}) (Alvis et al., 2009) over ventilated banking (estimated at 20–25 W m^{-2} K^{-1}) (Safari et al., 2018). In the case of coffee, a temperature usually above 200 °C, linked to roasting, may boost the AA content.

Chestnut-based baked goods represent an alternative to conventional wheat-based snacks. From a compositional perspective, chestnut flour is prone to AA formation due to its high fAsn content (Mesias & Morales, 2025). Therefore, the kinetic constant k_s in Eq. (1) is expected to be favoured. However, chestnut flour also exhibits a water-holding capacity of 463 g water per 100 g flour, markedly higher than the 84 g water per 100 g flour reported for wheat flour. This elevated water retention may delay water evaporation, counteracting the optimal conditions for AA formation (Mesias & Morales, 2025).

Once AA synthesis was recognised as a surface phenomenon, researchers explored non-contact predictive approaches for its quantification, aiming to avoid time-consuming and expensive analytical determinations and to develop systems feasible for in-line monitoring. Over the past two decades, colour and hyperspectral imaging (HSI) have established themselves as prominent non-contact, non-destructive techniques for AA prediction in heated foods. In bakery products, the browning index (BI) (Hirschler, 2012) or CIELab colour parameters, particularly lightness (L*) and the green–red balance (a*), are commonly used as indicators of AA risk (Gökmen et al., 2008; Isleroglu et al., 2012; Verma & Yadav, 2022). Although AA itself is colourless, its formation is associated with Maillard and caramelisation reactions, which produce colour changes that correlate with AA accumulation.

HSI exploits cameras with high spectral resolution, operating from the visible to the infrared regions (Xie et al., 2023), and has been successfully applied to products such as potatoes and coffee (Jar et al., 2025; Xie et al., 2024). HSI records the spectral pattern of light reflected from the product surface. The resulting spectra are primarily shaped by the matrix's chemical composition and crust components. For example, surface WC, Maillard reaction products, sugar caramelisation compounds, and other secondary reaction products are strongly associated with the actual AA content.

However, applications to baked foods remain limited. This scarcity of studies may be attributed to the wide variability in flour types, ingredient composition (e.g., leavening agents, eggs, milk), and product formats, including differences in shape, texture, porosity, glazing, and overall structure. More specifically, no studies have explicitly addressed the effect of shape and texture in baked products; therefore, product geometry may strongly influence the previously mentioned crust-based model of AA formation.

Recently, several depth-sensing technologies and three-dimensional (3D) analysis techniques have been developed and successfully applied in the food sector (Li et al., 2026). Properly designed 3D sensors, such as depth cameras, combined with image analysis algorithms (e.g., photogrammetry), represent powerful tools for sizing and categorising products. In addition, 3D analysis enables precise characterisation of food morphology, allowing accurate measurement of volume, surface area, and surface roughness. Consequently, 3D analysis may support the investigation of AA patterns by providing a detailed morphological assessment of baked foods.

Currently, the standard destructive methodology for AA quantification involves gas or liquid chromatography for molecule isolation, followed by mass spectrometry or ELISA determination (Mollakhalili et al., 2021). Mass spectrometry represents the most accurate, but also the most expensive, analytical technique; in bakery products, an error of approximately 2% has been reported (Mioara & Culetu, 2016). In contrast, for rapid, cost-effective screening, commercial ELISA kits are recommended, although their analytical error is typically around 20% (Life Technologies Pvt. Ltd., India). As a consequence, mass spectroscopy is a quantitative analysis, whereas ELISA works as a qualitative risk indicator.

The present study investigates the relationship between AA accumulation and the shape of baked foods using a single chestnut-based biscuit recipe. While contactless approaches, such as colour and hyperspectral imaging, are widely used for AA prediction, their performance may be limited in dark matrices, such as chestnut dough. At the same time, shape variability is a common issue that has been scarcely investigated, despite being a relevant source of variability in industrial production. To address this gap, four non-contact sensing techniques were evaluated: HSI, CIELab colour analysis, thermal imaging, 3D analysis. Thermal imaging was used to characterise surface temperature distribution, given the expected localisation of AA in the hottest regions. 3D analysis is enabled by photogrammetric reconstruction, which generates 3D point clouds from multiview colour images. 3D analysis provides essential descriptors potentially relevant to AA prediction, including product height, volume, and surface area from different shapes.

The objective of this study was thus to assess whether shape-related descriptors can improve AA prediction and to evaluate their contribution relative to other sensing approaches in a dark, under-investigated bakery matrix.

2. Materials and methods

2.1. Biscuits preparation and experimental design

A 400 g dough was prepared following a typical Italian recipe inspired by products typical of marginal mountainous areas of the Tuscan–Emilian Apennines (locally referred to as "Castègni"). The recipe consisted of 120 g chestnut flour, 60 g refined wheat flour, 90 g sucrose, 80 g sunflower oil, 30 g water, and 20 g sodium bicarbonate. The dough was mixed manually by the same operator for 6 min until homogeneous (i.e., all the flours were fully combined with the dough), then rested for 10 min before being divided into 16 portions of 25 g each (mean 25.045 ± 1.744 g). The portions were shaped into four biscuit geometries using specific cutters: Round, Striped, Star, and Irregular. The dough was levelled to a fixed height for Round, Striped, and Star at 6.6 mm, 7 mm, and 6.5 mm, respectively. In Striped-shaped biscuits, the stripes measured 2.5 mm in depth. In these groups, the geometry was controlled to assess mainly the shape effect. For irregular biscuits, a small dough ball was first formed, then manually flattened; hence, within-group variability was enhanced to simulate format variability. Four biscuits, one per shape, were placed on a tray and baked at 180 °C in a laboratory-ventilated oven, model TCN50 (Giorgio Bormac S.R.L., Carpi, Italy), for different durations (10, 18, 26, and 41 min). Five independent doughs were prepared, portioned into the four shapes, and baked, yielding five independent replicates with tray positions rotated at each repetition. All biscuits were weighed before and after baking. The experimental design followed a multifactorial randomised block design in which two factors, namely biscuit shape (Shape) and baking time (Time), were replicated five times. Finally, to describe the AA content as a function of baking time, a pseudo-first-order kinetic model reported in the literature was selected and is presented in Eq. (2) (Hsu et al., 2016).

$$AA_t = AA_\infty * \left(1 - e^{-ke*t}\right) \tag{2}$$

Where AA_t is the estimated AA content (μg kg^{-1}), AA_∞ represents the asymptotic value approached at long baking times (equilibrium) under the investigated conditions (μg kg^{-1}), k_e is the experimental reaction rate coefficient (min^{-1}), and t is the baking time (min). The model assumes that AA formation follows a monotonic accumulation towards a plateau, with negligible degradation under the selected baking conditions (180 °C). This assumption is consistent with the expected temperature range for AA degradation and is further supported by the absence of systematic trends in the model residuals over time.

2.2. Thermal analysis

After baking, the biscuits were placed in a dark box, laid on a green background, and monitored with a FLIR T560 thermal camera (Teledyne FLIR LLC, Wilsonville, OR, USA) positioned perpendicular to the samples at 650 mm. The camera operated in video mode, recording at 30 Hz with a thermal resolution of 640 × 480 pixels and a stated accuracy of ±2 °C, with an emissivity set to 0.93. The cooling behaviour of the biscuits was monitored for 40 min following removal from the oven. Surface temperature data were acquired using FLIR Research Studio software. For each biscuit, a region of interest (ROI) was manually defined by the same operator using the visible temperature gradient along the biscuit boundary to isolate the biscuit surface for the computation of thermal statistics. Details of biscuit placement and thermal data acquisition are shown in Fig. 1. For each frame, the mean, mode, maximum, minimum, and standard deviation (SD) of the surface temperature within each biscuit were calculated.

For the present study, only 2 time points were retained for the analysis: immediately after the baking (0 s) and after 90 s of cooling. The reported values correspond to the average of five consecutive frames for each selected time point. A 90 s resting period was selected to enhance the surface temperature heterogeneity generated during the early cooling phase (Takacs et al., 2020). Immediately after baking, the biscuit surface exhibited an almost homogeneous temperature distribution, whereas short-term cooling generated spatial temperature gradients related to biscuit geometry and surface structure. Hence, the coefficient of variation was computed as the ratio between SD and average temperature at different acquisition times, and the superficial temperature pattern at 90 s is representative of the cool-down phase.

2.3. Three-dimensional reconstruction

Four biscuits were arranged in a row on a green tray. Image acquisition was performed using a Canon R10 camera (Canon Inc., Tokyo, Japan) equipped with a 15–180 mm lens. Approximately 21 photographs were captured from above the biscuits at a fixed height of 300 mm, with the tray manually repositioned between successive images to obtain multiple overlapping views of the upper biscuit surfaces. The number of photographs was selected to achieve approximately 70% image overlap, ensuring reliable photogrammetric reconstruction. Image acquisition was conducted inside a lightbox (1 m side length) to ensure controlled and uniform LED illumination across samples. Colour calibration was performed by including a ColourChecker target in the first image; two markers were fixed on the tray for scaling. The images were processed using Metashape Professional 2.0.3 (Agisoft LLC, St. Petersburg, Russia) to generate 3D point clouds, following the standard workflow: Align Photos, Optimise Camera Alignment, and Build Dense Cloud. The reconstructed products were exported as a text file with six columns: the planar coordinates (X, Y), the vertical coordinate (Z, height), and the red (R), green (G), and blue (B) colour intensity values for each point.

2.4. Morphological evaluation

The point clouds exported as text files were processed using RStudio (version 2025.09.2, Posit Software, Boston (MA), U.S.). First, the green background was removed using pixel-level colour and depth classification with a k-nearest neighbours algorithm. Second, the point clouds were resampled onto a fixed X–Y grid with a resolution of 0.2 mm (namely, ΔX and ΔY equal to 0.2 mm), yielding approximately 72,000 points per biscuit on average. New points were generated by calculating the arithmetic mean of the X, Y, and Z coordinates and the R, G, and B values of all points falling within each grid cell. Subsequently, several 3D morphological parameters were calculated for each biscuit using dedicated R libraries, including Rvcg, Morpho, concaveman, sf, and lwgeom. The basic morphological parameters included the mean height (Zm) and the volume, calculated according to Eqs. (3) and (4). Zm and volume were approximated for the visible portion of the biscuit, namely

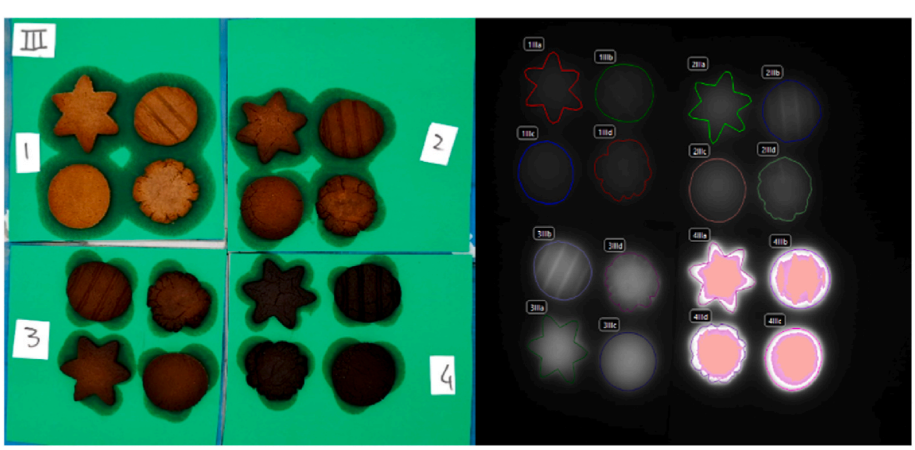

Fig. 1. On the left, a picture of the biscuits just out of the oven; on the right, a thermal image processing and data acquisition from a specific ROI per biscuit.

the lateral sides and the top face. Hence, the bottom face porosity was not included.

$$Zm = \frac{\sum Z_i}{n} \tag{3}$$

$$Volume = \Delta X * \Delta Y * \sum Z_i \tag{4}$$

The surface texture was characterised in terms of roughness and curviness, focusing on the top visible face of the biscuit. Based on the literature, food surfaces in direct contact with warm air play a crucial role in the baking mechanism and acrylamide synthesis (Yıldız et al., 2017). Hence, the bottom face, being in contact with the tray and less involved in convective heat exchange, was excluded. Roughness was quantified using three parameters: average absolute roughness (Ra), global roughness (Rg), and quadratic roughness (Rq). For Ra and Rg, a reference plane describing the upper biscuit height was fitted using a linear regression of the X and Y coordinates; Ra was calculated as the mean absolute deviation between the observed height (*Zi*) values for all points (*n*) and the fitted plane (Zl_i), whereas Rg corresponded to the root mean square of these deviations. In contrast, Rq was calculated as the root-mean-square deviation from a quadratic regression surface (Zq_i) to account for curvature trends across the biscuit surface (Hani et al., 2011). The formulas for the abovementioned indices are listed in Eq. (5–9).

$$Zl_i = \beta_0 + \beta_1 X_i + \beta_2 Y_i \tag{5}$$

$$Ra = \frac{\sum |Z_i - Zl_i|}{n} \tag{6}$$

$$Rg = \sqrt{\frac{\sum (Z_i - Zl_i)^2}{n}} \tag{7}$$

$$Zq_i = \beta_0 + \beta_1 X_i + \beta_2 Y_i + \beta_3 X_i^2 i + \beta_4 Y_i^2 + \beta_5 X_i Y_i \tag{8}$$

$$Rq = \sqrt{\frac{\sum (Z_i - Zq_i)^2}{n}} \tag{9}$$

The biscuit surface was approximated by fitting a triangular mesh to the point cloud vertices; consequently, the surface area (Surface) and further surface parameters were estimated only for the visible portion of the biscuit. SA:V was computed according to Eq. (10), recognising that it is not the actual surface-to-volume ratio but an index derived from the approximated volume and the contact interface between the food and the oven ambient. Mean curvature was calculated from the principal curvature values (k_1 *and* k_2) obtained from two orthogonal planes at each mesh vertex using the vcgCurve function. Specifically, the mean curvature (Hm) was computed as the average of k_1 and k_2 over all visible pixels (*n*), whereas the Gaussian curvature (Km) was calculated as the product of the two principal curvatures, following established methods for curvature estimation on triangular meshes. The formulas used are listed in Eq. (11–14).

$$SA : V = \frac{Surface}{Volume} \tag{10}$$

$$H_i = \frac{k_1 + k_2}{2} \tag{11}$$

$$Hm = \frac{\sum H_i}{n} \tag{12}$$

$$K_i = k_1 * k_2 \tag{13}$$

$$Km = \frac{\sum K_i}{n} \tag{14}$$

At this stage, all points were projected onto the X–Y plane to extract two-dimensional (2D) features. First, the perimeter was defined as the total length of the shape's contour. For each 2D shape, the major axis, the minor axis, and their ratio (AR) were computed. Finally, the concave area was defined as the surface of the 2D shape. In contrast, the convex area was derived from the junction of all external vertices of the 2D shape. Solidity was computed as the ratio of the concave to the convex areas. Regarding colour analysis, the R, G, and B values were converted to CIELab colour space indices (i.e., lightness (L*), red–green balance (a*), and blue–yellow balance (b*)) at each point. The mean and SD of the entire biscuit were computed for the three indices. The coefficient of variation (CV) was used to assess colour homogeneity within each biscuit, and it was computed using Eq. (15). Finally, the BI was determined using Eq. (16).

$$CV = \frac{\sqrt{\frac{\sum_i^n (x_i - \bar{x})^2}{n}}}{\frac{\sum_i^n x_i}{n}} \tag{15}$$

$$BI = 100 * \frac{\alpha - 0.31}{0.172}, \alpha = \frac{a^* + 1.75L^*}{5.645L^* + a^* - 3.012b^*} \tag{16}$$

Where n is the total number of points in each biscuit, x_i is the value of a colour index in each i-pixel, and $\bar{x}$ is the average value within a biscuit.

2.5. Morphological variable selection

A preliminary approach aimed to stress the biscuit's shape peculiar geometrical properties. Partial least squares discriminant analysis (PLS-DA) was applied to assess the relevance of the extracted morphological indices using variable importance in projection (VIP) scores. One-third of the indices exhibiting the highest VIP scores were selected for subsequent analyses. PLS-DA was used exclusively as an exploratory tool to reduce descriptor redundancy and identify shape-sensitive morphological features, rather than as a predictive model for acrylamide content. The relevant descriptors obtained from this analysis were selected for use in subsequent models for AA prediction.

2.6. Hyperspectral imaging and spectral analysis

Twenty-four hours after baking, the biscuits were analysed using a NIR hyperspectral imaging system operating in the 900–1700 nm range (Headwall Multi-Scan MV.V NIR; Headwall Photonics, Boston, MA, USA), mounted with a Computar ViSWIR Hyper APO 12 mm focal length lens M1218-APVSW2 (CBC Group LLC, NY, USA). The system was equipped with a push-broom scanner with 640 pixels and a spectral resolution of 4 nm and operated at a working distance of approximately 250 mm. The camera was mounted on a self-illuminated scanning slide equipped with two halogen lamps and controlled by dedicated software perClass Mira (perClass BV, Delft, Netherlands). System calibration was performed under completely dark conditions and using a white reference panel (Avian Technologies, Sunapee, NH, USA). The average absorbance spectrum within each biscuit was extracted. Spectral preprocessing began with the application of the standard normal variate (SNV) transformation to centre and scale the spectra. Subsequently, first-order (DI) and second-order (DII) Savitzky–Golay derivatives were calculated in RStudio using "prospectr" package. To reduce spectral dimensionality, mean reflectance and derivative values were resampled at 12 nm intervals. Wavelength selection was performed using partial least squares regression (PLSR) together with interval PLS (iPLS). Informative spectral regions were identified based on variable importance metrics while reducing redundancy caused by the strong autocorrelation between adjacent wavelengths. The SNV, DI, and DII datasets were evaluated both individually and in combination (SNV + DI and SNV + DII).

2.7. Acrylamide determination

Acrylamide was quantified using the Acrylamide ES ELISA kit in combination with a derivatisation kit, following the manufacturer's instructions (Gold Standard Diagnostics, Kassel, Germany) (Musa et al., 2024). Briefly, 2 g of the homogenised biscuit sample were mixed with 40 mL of distilled water. The mixture was continuously mixed for 30 min and then allowed to settle for 5 min. The resulting extract was filtered and subsequently centrifuged at 13,000 × g for 5 min. The supernatant underwent solid-phase extraction using multimodal chromatographic columns. Acrylamide was eluted from the columns with 1 mL of methanol/water (60:40, v/v), and the eluate was collected and repeated twice. The combined eluate was then heated to 50 °C for 60 min to allow derivatisation. After derivatisation, 2 mL of reaction buffer was added, and the samples were analysed according to the manufacturer's ELISA protocol. Absorbance was measured at 450 nm using a microplate reader (Tecan Infinite 200 Pro, i-control software; Männedorf, Switzerland). AA concentration was determined by comparison with a calibration curve generated using standard solutions at 0.0, 2.5, 5.0, 10.0, 25.0, 50.0, and 200.0 ng mL^{-1} (Gold Standard Diagnostics, 2021). The ELISA kit used for acrylamide quantification has a limit of detection (LOD) of 50 μg kg^{-1} for food samples. WC of the samples was determined by thermogravimetry using a microbalance.

2.8. Acrylamide prediction

AA data were first analysed using two-way analysis of variance (ANOVA) to evaluate the effects of baking time and biscuit shape and their interaction on AA content (formula: AA' $= \beta_0+\beta_1$Time$+\beta_2$Shape$+\beta_3$(Time×Shape)$+\epsilon$). At this point, AA concentration was then predicted (AA') using several multivariate linear regression (MLR) models, in which features from the hyperspectral, morphological, thermal, and colour datasets were used as predictors. An initial feature selection was performed within each data group; the final predictors were selected using forward-stepwise selection with AIC as the stopping criterion, restricting the number of variables to those yielding the highest coefficient of determination (R^2), the lowest root mean square error (RMSE), and the lowest AIC. The initial baseline MLR model was constructed using only essential hyperspectral wavelengths (Hyp). Model performance was subsequently improved by progressively incorporating additional classes of predictors: morphological (Morpho), colour (Lab), and thermal (Temp). The significance of the fitted models and their predictors was assessed through ANOVA and regression coefficient tests ($p < 0.05$). Only predictors that significantly contributed to the explained variance were retained in the final models. After MLR's development, predictive performance was evaluated using stratified five-fold cross-validation. Each validation fold includes one replicate for each combination of biscuit Shape and baking Time. Thus, at each iteration, 64 samples were used for model training (80%) and 16 for validation (20%). Model performance was evaluated on the validation dataset using the R^2, RMSE, and the mean absolute percentage error (MAPE), as reported in Eqs. 17 and 18 (namely: R^2cv, RMSEcv, and MAPEcv). Moreover, the Shapiro-Wilk test was used to assess the normality of the residual distributions for each model. Residuals were plotted for each variable to verify any sources of skewness.

$$RMSE = \sqrt{\frac{\sum (y_i - y_i')^2}{n}} \quad (17)$$

$$MAPE = \frac{100}{n} * \sum \left| \frac{y_i - y_i'}{y_i} \right| \quad (18)$$

Where y_i is the actual acrylamide content, and y'_i is the predicted one.

3. Results

3.1. AA content

AA content increased with baking time, and statistically significant differences were observed across the different shapes (to see Table A1). To evaluate the global effect of shape and baking time on acrylamide content, a two-way ANOVA was performed on the ELISA-derived data. Both main factors were highly significant ($p < 0.001$), confirming that AA accumulation is strongly influenced by both baking time and product geometry. In contrast, the interaction between shape and time was not significant ($p = 0.572$), indicating that the effect of shape is consistent across the investigated baking times. The model explained approximately 60% of the total variance ($R^2 = 0.60$). Variance partitioning showed that shape accounted for about 35% of the total variability, while baking time explained 24%. The interaction term contributed marginally (≈1%), with the remaining variance attributed to residual variability. This residual component is consistent with the use of ELISA as a reference analytical method, widely adopted for screening and associated with higher variability than confirmatory chromatographic techniques. Within this context, the observed unexplained variance reflects the intrinsic uncertainty of the ground truth used in this study. It indicates the upper limit of explainable variability expected in subsequent modelling approaches.

The recorded AA content at each bakery time was fitted to the pseudo-first-order kinetic model given in Eq. (2). The kinetics are depicted in Fig. 2a, one for each shape type. The ANOVA was performed on the coefficients of Eq. (2) (namely, AA_∞ and k_e), and shapes and outputs are listed in Table 1. No relevant statistical differences emerged from k_e. On the contrary, the Round shape exhibited the lowest AA_∞, while the Irregular shape exhibited the highest. Finally, WC decreased following first-order kinetics, approximated by a function with positive concavity (i.e., WC' $= \beta_0 + \beta_1 e^{(-\beta 2 time)}$). The average WC of the raw dough is 12.3 ± 0.7%, and it decreases to 4.9 ± 0.6%, 4.3 ± 0.6%, 4.1 ± 0.5%, and 3.8 ± 0.4% at 10, 18, 26, and 41 min of baking, respectively (Fig. 2b). As depicted in the chart in Fig. 2b, the lowest WC was recorded in Star and Striped shapes biscuits, especially when baked at 26 and 41 min. However, no statistically significant differences were found in the coefficients for the WC decrease kinetics function.

3.2. 3D products presentation and feature selections

Conventional morphological parameters obtained after baking are presented in Table 2. A preliminary feature selection was performed by training a PLS-DA model for shape prediction, analysing the morphometric traits as predictors. The model was built using eight predictors. The reduced feature model achieved an accuracy of 0.935 and a Cohen's kappa coefficient of 0.913 on a 5-fold cross-validation. The scores are plotted according to the first two components of the reduced PLS-DA model in Fig. 3a, while the VIP value for all variables is plotted in Fig. 3b. All the acronyms are listed in Table A2. A more robust validation was then performed using a single-way ANOVA to compare the most relevant and least autocorrelated morphometric traits across the four shape types. According to the feature selection process, Solidity and Rq emerged as the most relevant characteristics. A Tukey multiple-comparison test was subsequently applied to assess the distinctiveness of each trait within each shape type, and the results are depicted in Fig. 4. SA:V was included in Fig. 4a as the most frequently mentioned morphological index in the scientific review.

3.3. Colour

All three colour indices decreased with baking time. While L* and b* followed a trend parallel to the decrease in WC at each baking time, a* showed a three-step behaviour, with 10 min comparable to 26 min. The data are shown in Table 3. BI was not found to be informative under the

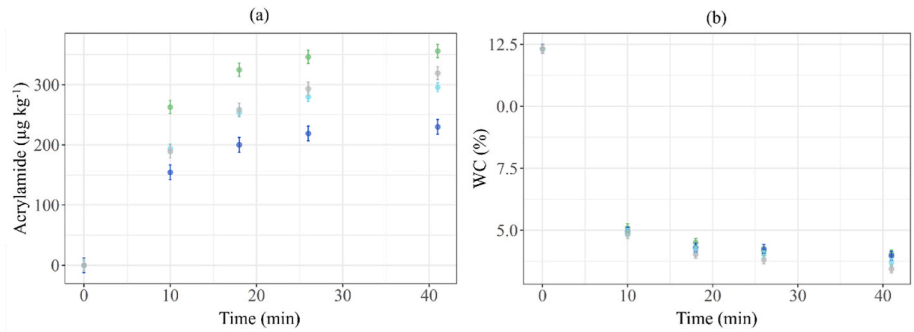

Fig. 2. Exponential function of AA content (μg kg^{-1}) in (a), and WC in (b) despite bakery time fitted on the experimental data, namely five repetitions, five bakery times (i.e., 0, 10, 18, 26, 41 min), and four kinds of shape: •Round, •Striped, •Star, and •Irregular. Error bars depict the standard error of the model computed within the five repetitions at each record.

Table 1
Coefficients AA_∞ and k_e derived from Eq. (2). Letters indicate statistical differences determined by the Tukey test.

Shape	AA_∞ (μg kg^{-1})	k_e (min^{-1})
Round	235.7 ± 38.1a	0.109 ± 0.031
Striped	329.2 ± 40.8b	0.095 ± 0.036
Star	304.5 ± 23.9b	0.112 ± 0.044
Irregular	367.0 ± 39.9c	0.129 ± 0.042

present experimental conditions. The mean colour indices did not vary among shapes; however, the average CV within biscuits was considerably lower in Round-shaped biscuits than in the other shapes.

3.4. Temperature

Essential temperature records are listed in Table 4. The data describe the mean temperature recorded at a specific time point, averaged across replicates. The CV was calculated across independent biscuit replicates to reflect pixel-level variability within individual biscuits. In addition, the ratio of pixels with a temperature above 120 °C to the total number of pixels within each ROI indicates the portion of the biscuit surface above 120 °C. An ANOVA was also performed on the temperature statistics. At the initial stage, no significant differences were observed among shapes; as expected, the mean and maximum recorded temperatures increased with baking time, except at 26 and 41 min, which were comparable. In contrast, differences emerged after 90 s of cooling, with Star-shaped and Irregular-shaped biscuits being cooler than Round-shaped biscuits. Finally, the surface proportion exceeding 120 °C was significantly affected by baking time, whereas no significant effect of biscuit shape was detected.

3.5. Wavelength selection

Based on the single-biscuit spectra reported in Fig. 5, the reflectance values were not proportionally shaped according to baking time. Neither the first derivative showed clear discrimination among baking durations (Fig. 5). This lack of clear discrimination suggests that acrylamide-related information is not confined to individual wavelengths but is distributed across the spectrum and partially masked by shape- and surface-related variability. Consequently, a multivariate approach was required to extract the relevant spectral information, and PLSR was applied. Based on the VIP assessment, for both SNV and DI, the key regions of the monitored spectrum were the lower wavelengths (below 1000 nm), a peak around 1200 nm, and the 1350–1450 nm range. The VIP score plots are shown in Fig. 6. Single wavelengths were then selected from each key region using iPLS analysis. The model that achieved the best performance for AA prediction, presented in Fig. 7a, combined the SNV and DI datasets and included nine components, yielding a cross-validation R^2 of 0.30 and a cross-validation RMSE of 61.23 μg kg^{-1}.

By reducing the predictors to a minimum number of features, an MLR model including the SNV reflectance at 1160 nm and the first derivatives at 1364 nm and 1556 nm achieved performance comparable to that of the aforementioned PLSR model, as shown in Fig. 7b. However, when the two most meaningful morphological traits identified in Section 3.2, namely Surface and Rq, were included, the MLR model improved, reaching an R^2 of 0.51 and an RMSE of 57.75 μg kg^{-1} (Fig. 7c).

3.6. Models' performance

Once the most meaningful features were identified for each data group, a series of MLR models was tested, and their performance was

Table 2
Conventional traits are reassumed from baked biscuits at progressively longer times. Average and SD of the weight, height (Zm), surface area, and volume (n = 5).

Shape	Baked (min)	Weight (g)	Zm (mm)	Surface (mm^2)	Volume (mm^3)
Star	10	22.336 ± 0.510	10.3 ± 2.1	3595.7 ± 145.9	31160 ± 5852
Star	18	21.983 ± 1.091	10.8 ± 1.3	3586.1 ± 585.1	30420 ± 3634
Star	26	21.832 ± 0.586	10.9 ± 1.7	3516.7 ± 507.2	30320 ± 3407
Star	41	20.840 ± 0.534	9.8 ± 1.5	3343.8 ± 274.9	27620 ± 4337
Striped	10	22.581 ± 1.827	9.8 ± 2.5	3919.1 ± 320.3	30300 ± 6884
Striped	18	21.521 ± 1.622	10.1 ± 1.1	3859.1 ± 195.5	30840 ± 2802
Striped	26	21.972 ± 1.128	10.7 ± 2.2	3917.8 ± 202.2	32260 ± 4941
Striped	41	21.467 ± 0.796	9.5 ± 0.8	3729.5 ± 212.4	28280 ± 1891
Round	10	22.248 ± 1.017	9.9 ± 2.7	3484.2 ± 141.6	30920 ± 7762
Round	18	21.78 ± 1.281	10.4 ± 2.1	3487.5 ± 180.4	32240 ± 5766
Round	26	21.644 ± 1.445	11.0 ± 2.0	3459.3 ± 108.4	33760 ± 5048
Round	41	21.403 ± 0.740	9.8 ± 1.4	3312.7 ± 153.2	29640 ± 3884
Irregular	10	22.935 ± 0.378	10.3 ± 2.1	3802.7 ± 185.9	30420 ± 6235
Irregular	18	22.191 ± 0.353	11.2 ± 1.8	3608.6 ± 271.6	32000 ± 6201
Irregular	26	22.055 ± 0.252	11.1 ± 2.2	3599.9 ± 222.8	30120 ± 4766
Irregular	41	21.459 ± 0.394	10.0 ± 0.8	3439.4 ± 259.0	27980 ± 2501

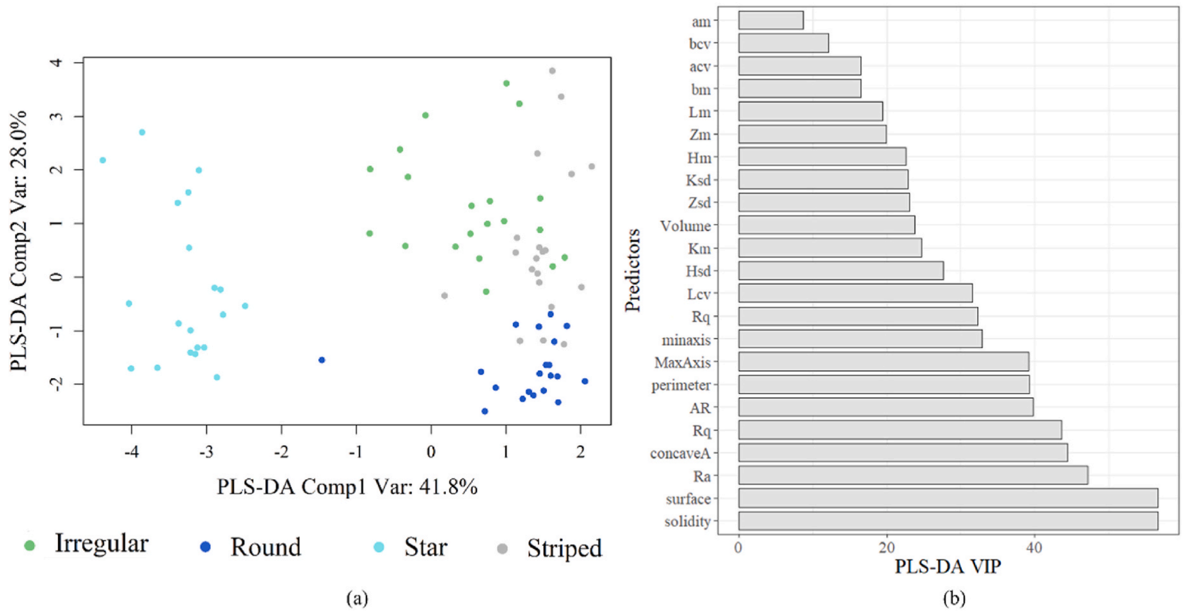

Fig. 3. a) Scores of each item plotted against the first and second components of the PLS-DA, performed on the morphological parameters and grouped according to their kind of shape; b) VIP for all the morphological parameters tested in the PLS-DA model, definitions are listed in Table A2.

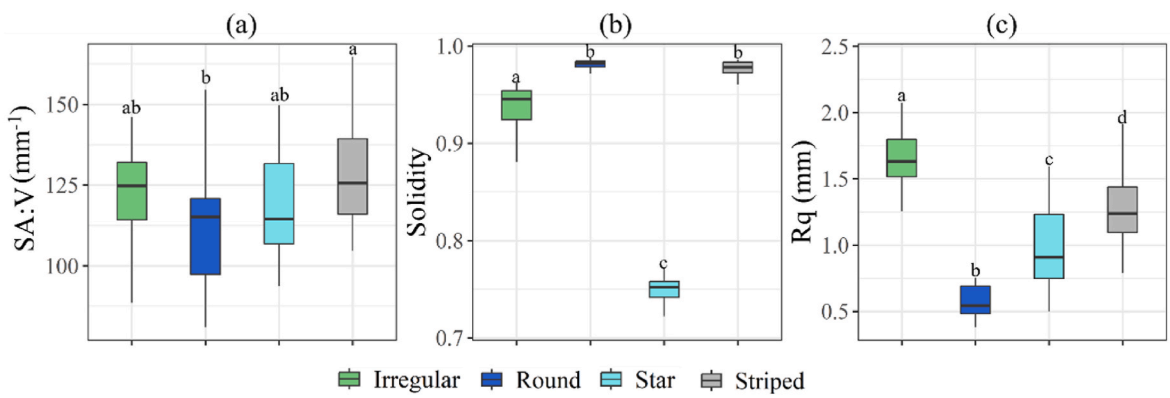

Fig. 4. Boxplots depict three morphological traits recorded for each shape type across five repetitions and four baking times (20 items per boxplot).

Table 3
CIELab indices are reassumed against shape and baking time. The mean is the average value across repetitions; the CV within each biscuit is averaged across repetitions (n = 5).

Shape	Baked	L*		a*		b*	
	(min)	Mean	Cv	Mean	Cv	Mean	Cv
Round	10	33.7	0.145	16.2	0.318	28.3	0.100
Round	18	23.5	0.239	15.8	0.315	21.1	0.230
Round	26	15.2	0.275	11.0	0.422	12.5	0.329
Round	41	10.7	0.278	6.0	0.700	5.3	0.341
Striped	10	31.6	0.162	15.5	0.303	27.1	0.091
Striped	18	22.1	0.229	15.2	0.298	20.2	0.209
Striped	26	15.3	0.290	11.1	0.435	12.2	0.292
Striped	41	9.8	0.357	5.7	0.822	4.8	0.419
Star	10	31.3	0.182	15.6	0.382	27.5	0.130
Star	18	22.3	0.247	14.9	0.359	20.3	0.251
Star	26	16.3	0.275	11.1	0.475	13.0	0.344
Star	41	10.3	0.311	5.2	1.012	4.8	0.477
Irregular	10	33.7	0.198	14.8	0.355	27.9	0.123
Irregular	18	23.1	0.275	14.6	0.380	21.1	0.245
Irregular	26	15.1	0.339	10.7	0.518	12.4	0.337
Irregular	41	10.2	0.360	5.5	0.891	5.1	0.411

Table 4
Mean, maximum, and CV of temperatures within each biscuit averaged among repetitions (n = 5).

Shape	Baked	Initial		90′		Surface > 120 °C
	(min)	Mean	CV	Mean	CV	
Irregular	10	95.4	0.043	67.2	0.059	0.00
Irregular	18	115.0	0.069	79.1	0.207	0.27
Irregular	26	125.0	0.081	88.3	0.096	0.84
Irregular	41	126.0	0.079	92.2	0.062	0.87
Round	10	97.2	0.043	71.6	0.061	0.00
Round	18	117.0	0.067	89.8	0.074	0.43
Round	26	126.0	0.077	112.0	0.098	0.86
Round	41	126.0	0.077	96.3	0.064	0.88
Star	10	95.4	0.045	68.4	0.076	0.00
Star	18	115.0	0.076	82.7	0.090	0.32
Star	26	123.0	0.092	85.6	0.100	0.79
Star	41	125.0	0.093	92.7	0.084	0.82
Striped	10	97.2	0.048	72.7	0.062	0.00
Striped	18	117.0	0.074	89.4	0.080	0.40
Striped	26	125.0	0.080	98.0	0.114	0.83
Striped	41	126.0	0.078	95.1	0.055	0.87

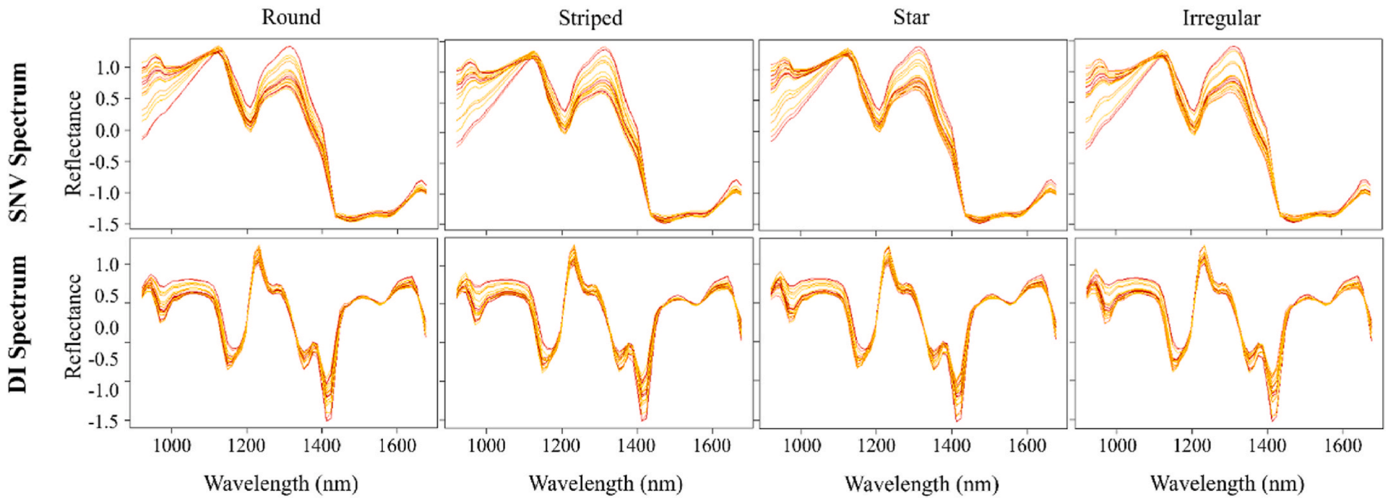

Fig. 5. The reflectance spectrum of each kind of shape is presented, from left to right: Round, Striped, Star, and Irregular-shaped. In the top row, the SNV spectra are displayed, while the DI spectrum is displayed on the bottom row. The colour of the line means the baking time: —10 min, —18 min, —26 min, —41 min. (For interpretation of the references to colour in this figure legend, the reader is referred to the Web version of this article.)

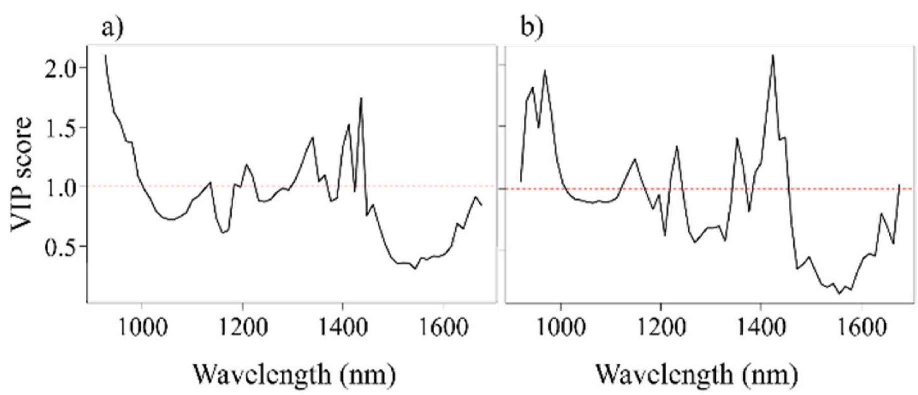

Fig. 6. VIP score derived from the PLSR: a) wavelengths from the SNV dataset, b) wavelengths from the DI dataset. The red-dashed line traces a score of 1, used as a preliminary threshold. (For interpretation of the references to colour in this figure legend, the reader is referred to the Web version of this article.)

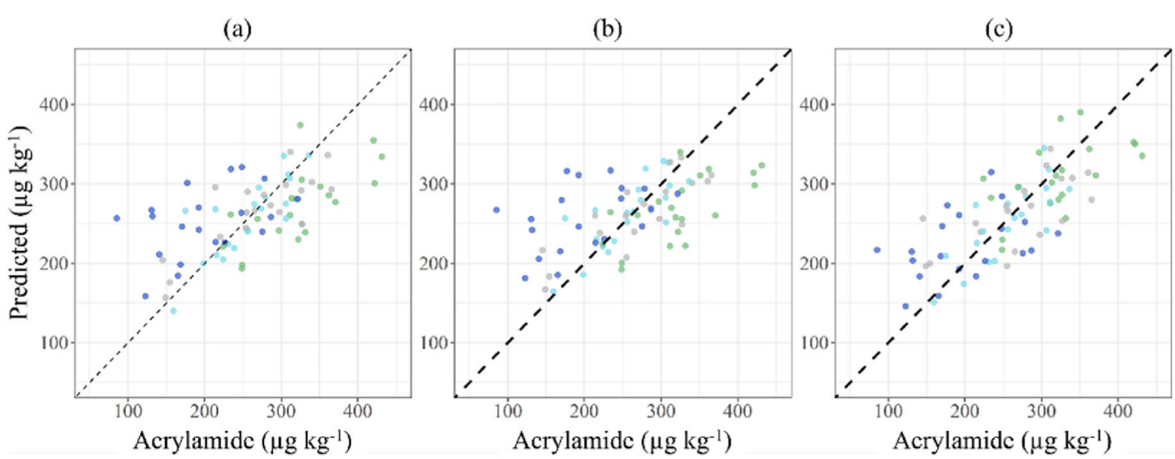

Fig. 7. The scatterplots depict the actual and predicted AA resulting from the PLSR model run on the SNV and DI datasets (a), the MLR model using only three essential wavelengths (b), and an MLR model including wavelengths and morphological traits (c), among four kinds of shape: •Round, •Striped, •Star, and •Irregular.

compared. All the tested models are listed in Eq. (19–26), and the acronyms' descriptions are reported in Table 5, while the models' performances on the validation dataset are compared in Table 6. The models' performances are quite similar, underscoring the relevance of each dataset type for predicting AA. However, Lab and Morpho performed best among the tested models for AA' prediction. Fig. 8 shows the comparison between the AA and AA' from all the items ($n = 80$) in some relevant MLR models and coloured by the biscuit's shape.

Table 5
The meanings of the acronyms used in Eq. (19–26) are listed here, grouped by the analysis technique they originated from.

Kind of data	Acronym	Meaning	Unit
Hyperspectral	SNV1160	Reflectance of a biscuit normalised at SNV	Normalised reflectance
	DI1364	First derivative of the SNV spectrum at that wavelength	Normalised reflectance
	DI1556	First derivative of the SNV spectrum at that wavelength	Normalised reflectance
Colour	Lsd	SD L superficial within each biscuit	NA
	bm	Mean b superficial value from each biscuit	NA
Temperature	TSsd	SD of the superficial temperature within each biscuit at the start of the monitoring	°C
Morphology	Rq	Quadratic roughness	mm
	Surface	Surface area of the biscuit's visible part	mm^2

Table 6
The performances retrieved from the validation test (n = 16) of the MLR models used in Eq. (19)–26 for AA prediction are presented.

Model	R^2cv	RMSEcv ($\mu g\ kg^{-1}$)	MAPEcv (%)
Hyp	0.33	56.7	21.5
Hyp, Morpho	0.44	51.2	19.4
Lab	0.36	52.4	19.9
Lab, Morpho	0.55	44.6	16.9
Lab, Hyp, Morpho	0.51	43.3	17.9
Lab, Temp	0.36	52.7	20.0
Lab, Temp, Morpho	0.54	45.2	17.1
All	0.51	48.1	18.2

$$Hyp : AA' = \beta_1 SNV1160 + \beta_2 DI1364 + \beta_3 DI1556 + \beta_0 \tag{19}$$

$$Hyp, Morpho : AA' = \beta_1 SNV1160 + \beta_2 DI1364 + \beta_3 DI1556 + \beta_4 Rquad + \beta_5\ solidity + \beta_0 \tag{20}$$

$$Lab : AA' = \beta_1 Lsd + +\beta_2 bm + \beta_0 \tag{21}$$

$$Lab, Morpho : AA' = \beta_1 Lsd + \beta_2 bm + \beta_3 Rq + \beta_4\ Surface + \beta_0 \tag{22}$$

$$Hyp, Lab, Morpho : AA' = \beta_1 SNV1160 + \beta_2 DI1364 + \beta_3 DI1556 + \beta_4 Lsd + \beta_5 bm + \beta_6 Rq + \beta_7\ Surface + \beta_0 \tag{23}$$

$$Lab, Temp : AA' = \beta_1 Lsd + \beta_2 bm + \beta_3 TsdS + \beta_0 \tag{24}$$

$$Lab, Temp, Morpho : AA' = \beta_1 Lsd + \beta_2 bm + \beta_3 TsdS + \beta_4 Rq + \beta_5\ Surface + \beta_0 \tag{25}$$

$$All : AA' = \beta_1 Lsd + \beta_2 bm + \beta_3 TsdS + \beta_4 SNV1160 + \beta_5 DI1364 + \beta_6 Rq + \beta_0 \tag{26}$$

4. Discussion

The evolution of acrylamide concentration during baking followed pseudo-first-order kinetics behaviour, confirming that this trend also applies to these chestnut-based biscuits (Alessia et al., 2022; Van Der Fels-Klerx et al., 2014). The AA content of the present biscuits was approximately comparable to, or lower than, that reported for commercial products made with different types of flour (Mesías et al., 2019). In the current study, AA content ranged from 85.2 $\mu g\ kg^{-1}$ to 431.3 $\mu g\ kg^{-1}$. In other chestnut flour-based products, AA content ranged from 4 $\mu g\ kg^{-1}$ to 159 $\mu g\ kg^{-1}$ (Karasek et al., 2009). Direct comparisons should be interpreted with caution because the available studies differ in dough formulation, baking protocol, and analytical methodology. Notably, exceptionally high AA levels were not recorded even after 41 min of baking. One possible explanation is that the naturally occurring antioxidant compounds in chestnut flour may partially limit AA formation (Donno et al., 2023; Mesias & Morales, 2016). Similarly, the high water-holding capacity of chestnut flour may have delayed surface dehydration, thereby reducing the conditions favourable for AA formation (Mesias & Morales, 2025). Alternatively, the selected baking temperature or baking system may not have sufficiently promoted AA formation (Ahmad et al., 2022; Açar & Gökmen, 2010). In the present experimental design, biscuit shape accounted for the largest part of the observed variability. The present findings are consistent with the crust model proposed by (Gökmen et al., 2008), which suggests that heat-sensitive boundaries and surface ripples on Irregular and Striped biscuits promote AA synthesis, on average. As shown in Section 3.1, analysis of the AA kinetics (Eq. (2)) among shapes showed that shape did not affect the rate of increase in AA (ke); instead, it appeared to have a primary effect on the AA_∞ owing to its geometrical traits, with the Round shape recording the lowest AA_∞ (Table 1) because of its more compact geometry. Fig. 9 illustrates the structure of a representative sample from each shape type. The Round biscuit (Fig. 9a) has the most regular shape and a nearly uniform surface texture. In the Striped biscuit, the texture follows the stripe pattern, which is visible both in the

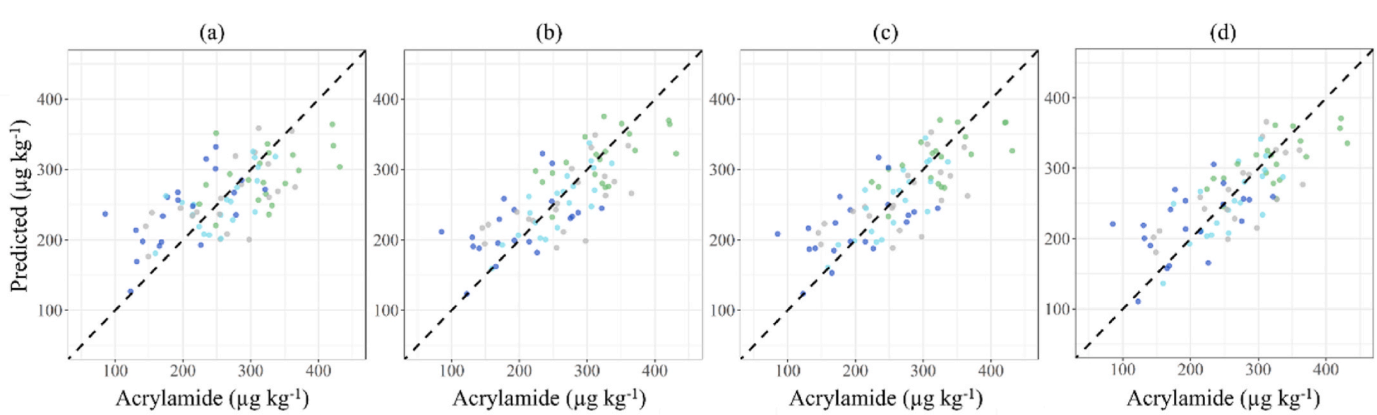

Fig. 8. The scatterplots depict the actual and predicted AA values from the most prominent MLR models: a) Lab, b) Lab, Morpho, c) Lab, Temp, Morpho, d) Lab, Temp, Hyper, Morpho. The black-dashed line represents the perfect regression. Colours referred to the kinds of shapes: •Round, •Striped, •Star, and •Irregular. (For interpretation of the references to colour in this figure legend, the reader is referred to the Web version of this article.)

cross-section and in the depth map in Fig. 9b. In the Star- and Irregular-shaped biscuits (Fig. 9c and d), depressions are concentrated in the biscuit's centre, while peaks surround the biscuit border. These morphological differences provide a plausible explanation for the heterogeneous heat distribution observed during baking and, consequently, for the spatial variability of AA accumulation.

Given the promising results reported in the literature on the use of HSI for AA prediction, the evaluation began with this technique. The wavelengths selected in the present study were close to those previously reported, except for 1364 nm, which may reflect a different interaction with the matrix under investigation. Wavelengths around 1360 nm have previously been associated with the stretching vibrations of water molecules in starch-based products (Malegori et al., 2022; Zhang et al., 2023). Wavelengths of 888 nm and 1123 nm have also been reported for roasted coffee, together with bands around 1450 nm and 1630 nm (Xie et al., 2024), whereas key wavelengths at 1430, 1520, and 1630 nm were identified in potatoes (Jar et al., 2025). The best-performing PLSR model also combined the SNV and DI datasets for AA prediction, consistent with the findings of Jar et al. (2025). However, the predictive performance achieved in the present study was lower than that reported for coffee (external validation R^2cv = 0.81, RMSEcv = 37.4 μg kg^{-1}, mean AA = 268.3 μg kg^{-1}) and potatoes (R^2cv = 0.82, RMSEcv = 219 μg kg^{-1}, mean AA = 727 μg kg^{-1}) (R^2cv = 0.89, RMSEcv = 733.8 μg kg^{-1}; AA range = 233–3363 μg kg^{-1}). Direct comparisons should be interpreted with caution because the concentration ranges and food matrices differed substantially among studies. Nevertheless, despite the large number of spectral variables included in PLSR models, only three selected wavelengths were sufficient to achieve an acceptable AA prediction using MLR after feature selection. Therefore, the data acquisition procedure and spectral analysis followed a well-established methodology, suggesting that bakery products may represent a challenging matrix for HSI. Under the investigated conditions, the additional spectral information provided by hyperspectral imaging did not translate into a substantial improvement in AA prediction compared with models based solely on CIELab colour features. The biscuit geometry and the intrinsic characteristics of the matrix are likely to interfere with hyperspectral signal acquisition, thereby affecting the consistency of surface reflectance. A possible explanation is that HSI may primarily captures the overall moisture-loss process occurring at the product surface, whereas AA accumulates locally in hotspots that have reached the activation energy required for its formation. This may explain why local AA accumulation continues within these hotspots according to its kinetic behaviour (Eq. (2)), while HSI predominantly reflects the average spectral properties of the entire surface. Moreover, matrix-related interferences, including light scattering and background reflectance, have been reported to substantially affect absorbance measurements when detecting localised contaminants (Ma et al., 2019; Soni et al., 2022). However, based on the experimental design of the present study, it was not possible to isolate and quantify the specific contribution of biscuit shape to hyperspectral variability. Nevertheless, incorporating a morphological predictor into the best-performing Hyp, Morpho-MLR provided a modest improvement, increasing R^2cv from 0.33 to 0.44 while reducing the MAPEcv from 20.5% to 19.4%.

Although HSI showed limited performance in AA prediction, surface colour proved the most informative source of data, even in dark doughs such as chestnut-based biscuits. Beyond the established relevance of the L* index for AA prediction (Sepehr et al., 2026), the present study suggests that the b* index is more important than a*, which is traditionally more closely associated with surface browning (Gökmen et al., 2008). Because the raw dough is inherently brown, its dark colour may have increased the sensitivity of b* more sensitive to colour changes occurring during baking in this type of product. Indeed, the average L* and b* values were strongly correlated with baking time. Moreover, their within-biscuit variability, assessed by the coefficient of variation (Lcv and bcv), was closely associated with AA content. Pronounced colour variability may indicate clusters of pixels on the biscuit surface where the conditions for AA formation are particularly favourable (i.e., rapid dehydration and intense hot-air exposure). This local surface heterogeneity may have been captured more effectively by colour analysis than by HSI. Compared with HSI, the CIELab analysis provided a higher spatial resolution (25 pixels mm^{-2} versus 11.1 pixels mm^{-2}). Although the colour images were resampled to optimise the generation of the point clouds, their native spatial resolution remained substantially higher than that of the HSI images. Consequently, the colour analysis may have preserved small-scale surface features that were smoothed in the HSI. This interpretation is supported by the superior performance of the Lab-MLR adding with the Hyp-MLR. Moreover, incorporating the Hyp predictors into the Lab, Morpho MLR (colour and morphological predictors) did not improve predictive performance. On the contrary, MAPEcv slightly increased from 16.9% to 17.9%, and R^2cv slightly increased from 0.55 to 0.51, indicating that the additional spectral information did not provide complementary predictive value.

Among the thermal descriptors evaluated, only the within-biscuit surface temperature SD was retained in the final prediction models. Whereas the mean surface temperature represents the overall thermal state of the biscuit, SD primarily reflects temperature variability. Due to the complex geometry and variable surface texture of the baked product,

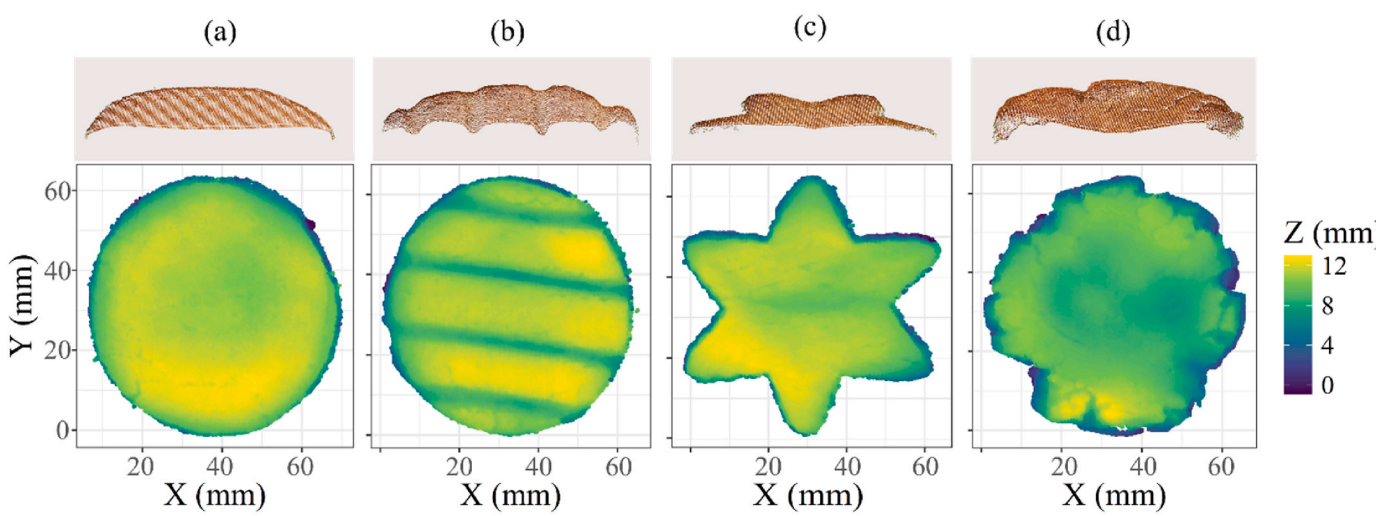

Fig. 9. The first row collects cross-sections from four sampled biscuits baked for 10 min. The second row collects the depth map according to the X, Y, and Z coordinates, currently scaled. Z equal to 0 means the tray level. (a) represents a Round biscuit, (b) Striped, (c) Star, (d) Irregular.

the surface temperature cannot be uniform. Accordingly, AA is unlikely to be evenly distributed across the biscuit surface and is expected to accumulate preferentially in the hottest regions. In this context, surface temperature variability may represent a particularly informative predictor of AA accumulation. Nevertheless, incorporating thermal predictors into the MLR models provided only a limited improvement in prediction performance compared with the combination of colour and morphological descriptors. This limited improvement suggests that the thermal information was largely already encoded in the colour and morphological descriptors, which integrate the cumulative effects of heating, dehydration, browning, and local surface geometry during baking.

Although combining conventional non-contact analytical techniques provided only limited improvements in AA prediction, the inclusion of 3D morphological descriptors substantially enhanced model performance in assessing AA accumulation in bakery products. The current scientific literature has primarily focused on total mass and product thickness, from which the SA:V is derived (Manley & Clark, 2011). In the present study, however, SA:V was almost comparable across shapes, whereas AA content varied consistently. Instead, subtle differences in biscuit geometry were captured by specific descriptors, such as Rq and Surface, which consistently improved the MLR models (i.e., all models labelled as "Morpho"), with the Lab, Morpho-MLR achieving the best overall performance. This model returned a MAPEcv of 17%, which is comparable with the uncertainty typically reported for commercial ELISA kits (≈20%). The superior performance of the Lab, Morpho-MLR may be explained by three factors. First, colour and 3D features were acquired at the highest spatial resolution among the evaluated techniques, allowing the finest surface details of the biscuit matrix to be captured. Indeed, the spatial resolution of the evaluated techniques was approximately 25 pixels mm^{-2} for colour and 3D analysis, 11.1 pixels mm^{-2} for HSI, and only 1.6 pixels mm^{-2} for thermal imaging. Second, as reported in Section 3.2, these descriptors effectively differentiated biscuit shapes; specifically, Rq was directly selected as a relevant feature, while Surface contributed to the calculation of Solidity, which was also identified as a relevant descriptor for shape discrimination. Third, according to the crust model of AA formation, Rq and Surface describe the superficial texture of baked products: surface reflects the amount of active substrate available per biscuit, whereas Rq characterises the spatial conformation of the biscuit surface. Indeed, Irregular and Striped biscuits exhibited the highest Rq values, whereas the Round shape showed the lowest. The surface and border characteristics from which Rq and Surface were derived are illustrated in Fig. 9. Rougher surfaces may promote AA accumulation through several mechanisms, including an increased active surface area, the formation of regions prone to faster dehydration, and enhanced convective heat transfer due to greater airflow over the surface (Alessia et al., 2022). Therefore, a detailed quantitative description of biscuit texture may represent an important advancement for AA prediction in bakery products with variable geometries. Previous studies have mainly focused on dough formulation or baking temperature, whereas the effect of product shape has received little attention. As previously discussed, ingredients such as different flours or AA-reducing additives (e.g., sodium chloride or antioxidants) primarily influence the activation energy required for AA formation, while higher baking temperatures provide additional energy to activate the reaction pathways. These factors mainly affect the rate of AA formation. In contrast, biscuit shape did not significantly influence the apparent reaction rate constant (ke), indicating that geometry does not alter the intrinsic kinetics of AA formation under the investigated conditions. As shown in Fig. 2, the curves corresponding to the different shapes are essentially parallel, whereas the maximum attainable AA content differs among shapes because different geometries expose different portions of the biscuit surface to conditions favourable for AA formation. Consequently, a higher AA plateau (AA_∞) cannot be attributed to an increased synthesis rate (ke), since all biscuits were prepared from the same dough and baked under identical conditions. Instead, the differences among shapes are more likely associated with differences in surface heating and dehydration before the activation threshold for AA formation is reached. In certain geometries, faster surface warming and dehydration may prepare a larger proportion of the surface for AA formation, thereby increasing the maximum attainable AA concentration. Consequently, future strategies for mitigating AA formation may benefit more from limiting local surface overheating (Ahrne et al., 2007; Isleroglu et al., 2012) than from attempts to modify the intrinsic kinetics of AA formation alone.

As a further outcome of the comparison among the four contactless analytical techniques, the best-performing predictive model relied exclusively on data acquired from standard RGB sensors, making it suitable, at least, for preliminary AA screening. Both the biscuit surface colour and the images required for 3D reconstruction by photogrammetry were acquired using a conventional RGB camera. Although photogrammetry requires multiple images or a multiview acquisition system, together with dedicated hardware and software for post-acquisition image processing, it remains more cost-effective than other optical sensing technologies, such as HSI and thermal imaging. Moreover, RGB imaging requires only basic adjustments, such as light intensity and colour balance, whereas HSI systems require white- and dark-reference calibrations to ensure measurement reliability (Henriksen et al., 2022). Thermal cameras may also require periodic calibration. Although the Lab, Morpho model showed the best predictive performance under the investigated conditions, the combination of RGB imaging and photogrammetry appears to represent a promising monitoring strategy, providing a practical balance between prediction accuracy, implementation cost, and operational simplicity. Furthermore, RGB cameras are already widely installed above conveyor belts in modern bakery plants for routine product inspection. Compared with HSI and thermal imaging, RGB-based multiview imaging may offer greater flexibility for integration into existing industrial inspection lines, although dedicated hardware and synchronisation would still be required for reliable photogrammetric reconstruction of moving products.

In conclusion, the experimental results suggest that surface-related information and spatially resolved measurements are important for improving AA prediction. Considering that the "Lab, Morpho" model provided reliable predictions (Table 6) and that colour and height information are available point-by-point, the proposed approach was extended to estimate the spatial distribution of AA across the biscuit surface. Accordingly, the simplified "Lab, Morpho" model (Eq. (27)) was used to derive the coefficients for a second model that estimated AA content at each point using the local colour and roughness descriptors (namely Li*, bi*, and Rqi, where Rqi is the quadratic deviation of Zqi from Zi), while the whole-biscuit Rq and Surface values were included to account for the overall shape effect. Details are reported in Eq. (28).

$$AA' = \beta_1 L^* + \beta_2 b^* + \beta_3 Rq + \beta_4 (Rq * Surface) + \beta_0 \tag{27}$$

$$AAi' = \beta_1 Li^* + \beta_2 bi^* + \beta_3 Rqi + \beta_4 (Rq * Surface) + \beta_0 \tag{28}$$

The average RMSE of the point-by-point predictions reflected the performance of the whole-biscuit model (RMSE = 48.17 μg kg^{-1}, MAPE = 16.5%), with the highest average RMSE observed for the Irregular shape and the lowest for the Star shape. The resulting spatial predictions are presented in Fig. 10, where the progressive accumulation of AA is visible in both the Round and Irregular biscuits. Predictions for the Star shape are shown in Fig. 11a and b, whereas Fig. 11c and d presents the Striped biscuits. The aim of the point-by-point modelling was not to quantitatively reconstruct the local acrylamide concentration, but rather to provide a qualitative representation of regions more likely to favour AA accumulation. In particular, the biscuit borders and the protruding regions of the Star shape appear to be preferential sites for AA formation, whereas the valleys between the stripes exhibited lower predicted AA than the corresponding peaks. Similar spatial modelling approaches may support the future design of bakery products

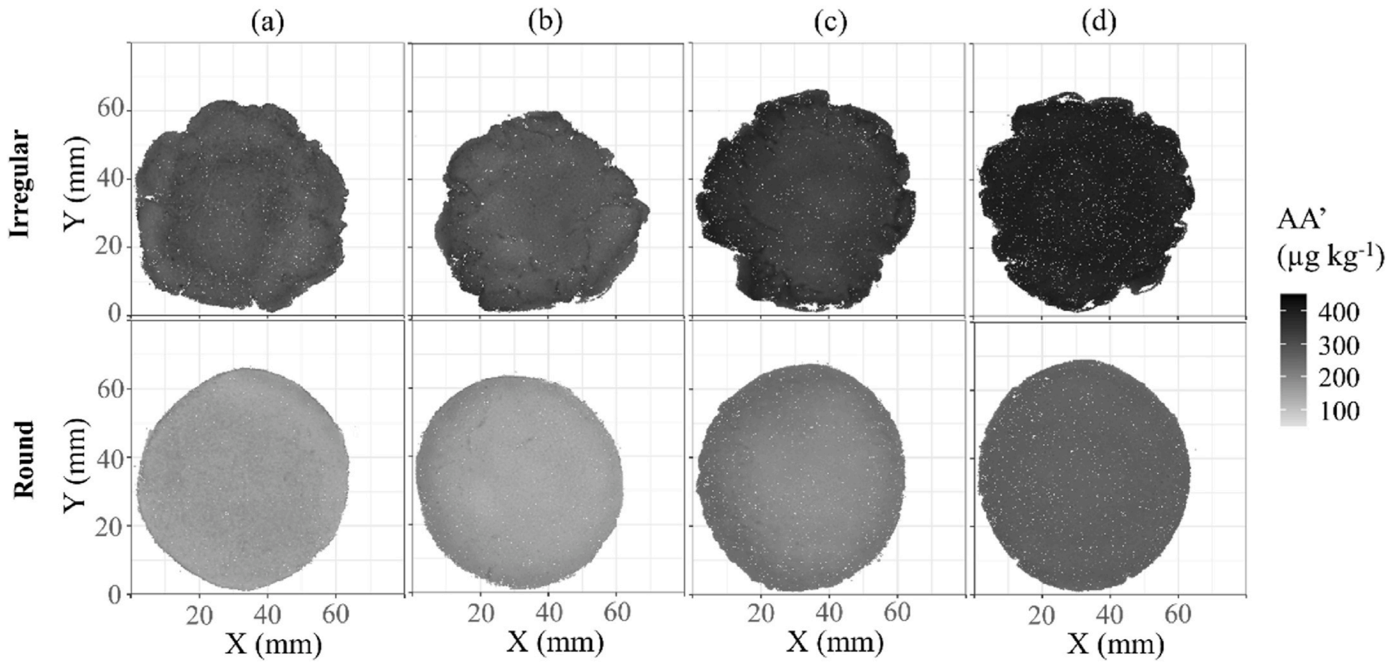

Fig. 10. AA' is mapped on the biscuit's surface. Irregular biscuits are collected in the top row and Round biscuits in the bottom row. Lettes indicate a baked time: (a) 10 min, (b) 18 min, (c) 26 min, (d) 41 min.

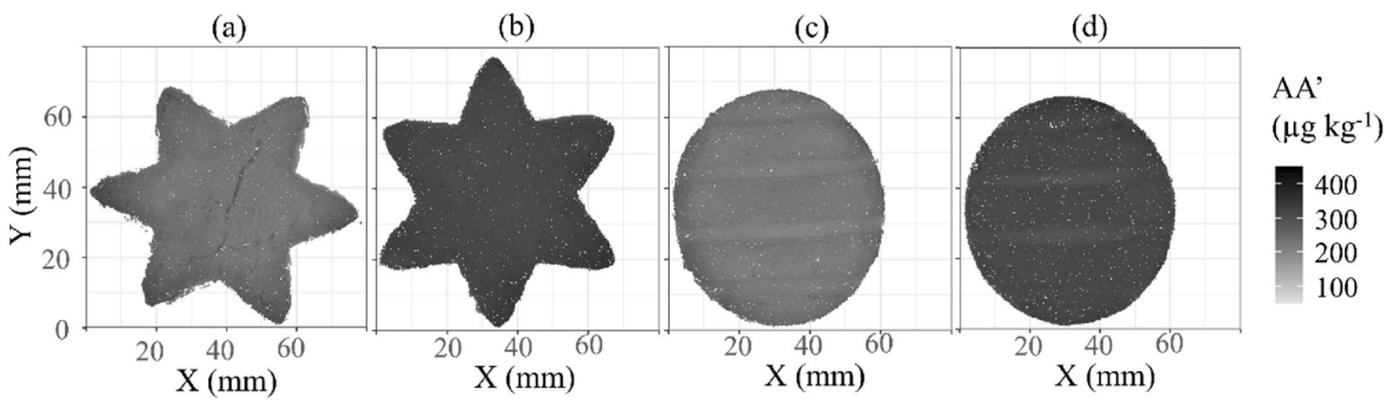

Fig. 11. AA' is mapped on the biscuit's surface. Star biscuits are collected in (a) and (b), Stripped biscuits in (c) and (d); moreover, (a) and (c) were baked at 18 min, (b) and (d) were baked at 41 min.

with geometries that are less prone to local AA accumulation. However, further experimental validation at the local scale will be required before this approach can be considered for practical applications.

5. Conclusions

In the present study, AA content in chestnut-based biscuits was investigated using non-contact sensing techniques. Four imaging-based sensing approaches were compared based on the hypothesis that the surface characteristics of baked products, which depend on their 3D geometry, may play an important role in AA formation. Under the investigated conditions, HSI showed lower predictive performance than previously reported for other food matrices, suggesting that its application to bakery products may require further optimisation or additional approaches to account for matrix-specific variability. Thermal monitoring of the biscuit surface provided only a limited improvement in AA prediction, whereas colour analysis, particularly lightness and the blue–yellow balance, yielded relevant predictive information. Morphometric evaluation based on 3D reconstruction further improved AA prediction by accounting for biscuit shape variability. In particular, surface roughness and the effective 3D surface area were associated with differences in predicted AA accumulation among biscuit geometries. Although chromatographic methods coupled with mass spectrometry remain the reference approach for AA determination, the proposed methodology may provide a rapid, contactless screening tool for online process monitoring, enabling the early identification of potential process deviations during production and supporting timely corrective actions.

CRediT authorship contribution statement

Alessandro Zanchin: Writing – original draft, Methodology, Investigation, Formal analysis, Data curation, Conceptualization. **Marco Napoli:** Writing – review & editing, Supervision, Formal analysis. **Antonio Pescatore:** Supervision, Formal analysis. **Nicolò Cecchin:** Methodology, Formal analysis, Data curation. **Lorenzo Guerrini:** Writing – review & editing, Supervision, Methodology, Investigation, Conceptualization.

Declaration of competing interests

The authors declare that they have no known competing financial interests or personal relationships that could have appeared to influence the work reported in this paper: "Acrylamide prediction on chestnut-based biscuits, a shaped matter".

The author is an Editorial Board Member/Editor-in-Chief/Associate Editor/Guest Editor for *Food Control* was not involved in the editorial review or the decision to publish this article.

Acknowledgements

This study was carried out within the Agritech National Research Center and received funding from the European Union Next-GenerationEU (PIANO NAZIONALE DI RIPRESA E RESILIENZA (PNRR)—MISSIONE 4 COMPONENTE 2, INVESTIMENTO 1.4—D.D. 1032 17/06/2022, CN00000022). This manuscript reflects only the authors' views and opinions, neither the European Union nor the European Commission can be considered responsible for them.

Appendix A. Supplementary data

Table A1
AA average content and SD.

Shape	Baking time (min)	AA (μg kg^{-1})
Round	10	145.7 ± 20.3
Round	18	207.8 ± 52.8
Round	26	228.3 ± 98.0
Round	41	220.0 ± 33.1
Striped	10	193.7 ± 60.8
Striped	18	262.6 ± 49.0
Striped	26	276.9 ± 54.4
Striped	41	328.2 ± 36.4
Star	10	210.3 ± 32.2
Star	18	233.4 ± 49.9
Star	26	275.1 ± 21.2
Star	41	306.9 ± 20.2
Irregular	10	272.9 ± 46.0
Irregular	18	314.5 ± 49.6
Irregular	26	330.4 ± 59.0
Irregular	41	373.1 ± 50.6

Table A2
Definition of acronyms reported in Fig. 3b.

Acronym	Definition
am	Average a* from CIELab
acv	CV of a* from CIELab within biscuit
bm	Average b* from CIELab
bcv	CV of b* from CIELab within biscuit
Lm	Average L* from CIELab
Lcv	CV of L* from CIELab within biscuit
Hm	Average mean curvature (H)
Ksd	Gaussian curvature (K) standard deviation
Zsd	Standard deviation of the biscuit's height
Volume	Measured biscuit's volume
Km	Average gaussian curvature (K)
Hsd	Averager curvature (H) standard deviation
Zm	Average biscuit's height
Rg	Global roughness
minaxis	Average length of the minimum axis
Maxaxis	Average length of the maximum axis
perimeter	Average biscuit's perimeter
AR	Average axis ratio
Rq	Quadratic roughness
concave_A	Concacave area
Ra	Average roughness
surface	Average surface area of biscuits
solidity	Average solidity

Data availability

Data will be made available on request.

References

Açar, Ö.Ç., & Gökmen, V. (2010). *A new approach to evaluate the risk arising from acrylamide formation in cookies during baking : Total risk calculation, 100* pp. 642–648). https://doi.org/10.1016/j.jfoodeng.2010.05.013

Ahmad, M. M., Qureshi, T. M., Mushtaq, M., Aqib, A. I., Mushtaq, U., Ibrahim, S. A., Rehman, A., Iqbal, M. W., Imran, T., Siddiqui, S. A., Javed, A., Shamim, S., & Saleem, M. H. (2022). Influence of baking and frying conditions on acrylamide formation in various prepared bakery, snack, and fried products. *Frontiers in Nutrition, 9*, Article 1011384. https://doi.org/10.3389/fnut.2022.1011384

Ahrne, L., Floberg, P., & Rose, J. (2007). *Effect of crust temperature and water content on acrylamide formation during baking of white bread : Steam and falling temperature baking* (Vol. 40, pp. 1708–1715). https://doi.org/10.1016/j.lwt.2007.01.010

Alessia, M., Tappi, S., Glicerina, V., Rocculi, P., Angeloni, S., Cortese, M., Caprioli, G., Vittori, S., & Romani, S. (2022). Formation of acrylamide in biscuits during baking under different heat transfer conditions. *LWT, 153*(September 2021), Article 112541. https://doi.org/10.1016/j.lwt.2021.112541

Alvis, A., Vélez, C., Rada-Mendoza, M., Villamiel, M., & Villada, H. S. (2009). Heat transfer coefficient during deep-fat frying. *Food Control, 20*(4), 321–325. https://doi.org/10.1016/j.foodcont.2008.05.016

Claeys, W. L., De Vleeschouwer, K., & Hendrickx, M. E. (2005). Kinetics of acrylamide formation and elimination during heating of an asparagine−sugar model system. *Journal of Agricultural and Food Chemistry, 53*(26), 9999–10005. https://doi.org/10.1021/jf051197n

Contaminants in the Food Chain (CONTAM), E. P. (2015). Scientific opinion on acrylamide in food. *EFSA Journal, 13*(6), 4104. https://doi.org/10.2903/j.efsa.2015.4104

Donno, D., Mellano, M. G., Carini, V., Bergamasco, E., Gamba, G., & Beccaro, G. L. (2023). Application of traditional cooking methods in chestnut processing: Effects of roasting and boiling on secondary metabolites and antioxidant capacity in Castanea spp. fruits. *Agriculture, 13*(3). https://doi.org/10.3390/agriculture13030530

European Commission. (20 November 2017). Establishing mitigation measures and benchmark levels for the reduction of the presence of acrylamide in food. *Official Journal of the European Union*, (2017/2158). http://data.europa.eu/eli/reg/2017/2158/oj.

Gökmen, V., & Açar, Ö.Ç. (2009). *Investigation of acrylamide formation on bakery products using a crust-like model*. https://doi.org/10.1002/mnfr.200800585

Gökmen, V., Açar, Ö.Ç., Arribas-Lorenzo, G., & Morales, F. J. (2008). Investigating the correlation between acrylamide content and browning ratio of model cookies. *Journal of Food Engineering, 87*(3), 380–385. https://doi.org/10.1016/j.jfoodeng.2007.12.029

Hani, A. F. M., Sathyamoorthy, D., & Sagayan Asirvadam, V. (2011). A method for computation of surface roughness of digital elevation model terrains via multiscale analysis. *Computers & Geosciences, 37*(2), 177–192. https://doi.org/10.1016/j.cageo.2010.05.021

Henriksen, M. L., Pedersen, W. N., Klarskov, P., & Hinge, M. (2022). One step calibration of industrial hyperspectral cameras. *Chemometrics and Intelligent Laboratory Systems, 227*, Article 104609. https://doi.org/10.1016/j.chemolab.2022.104609

Hirschler, R. (2012). Browning in food colorimetry. *Color in food: Technological and psychophysical aspects*.

Hsu, H.-T., Chen, M.-J., Tseng, T.-P., Cheng, L.-H., Huang, L.-J., & Yeh, T.-S. (2016). Kinetics for the distribution of acrylamide in French fries, fried oil and vapour during frying of potatoes. *Food Chemistry, 211*, 669–678. https://doi.org/10.1016/j.foodchem.2016.05.125

INTERNATIONAL AGENCY FOR RESEARCH ON CANCER (IRAC). (1994). ACRYLAMIDE (Group 2A). In *IARC monographs on the evaluation of carcinogenic risks to humans* (Vol. 60, pp. 389–435). International Agency for Research on Cancer (IARC). Some Industrial Chemicals.

Isleroglu, H., Kemerli, T., Sakin-Yilmazer, M., Guven, G., Ozdestan, O., Uren, A., & Kaymak-Ertekin, F. (2012). Effect of steam baking on acrylamide formation and browning kinetics of cookies. *Journal of Food Science, 77*(10), 257–263. https://doi.org/10.1111/j.1750-3841.2012.02912.x

Jar, C., Peraza-alem, C. M., Ignacio, J., Galarreta, R. De, Barandalla, L., & Arazuri, S. (2025). Mapping acrylamide content in potato chips using near-infrared hyperspectral imaging and chemometrics, 479(November 2024) https://doi.org/10.1016/j.foodchem.2025.143794.

Jensen, S. N., Hakme, E., & Feyissa, A. H. (2025). Kinetic modelling of acrylamide formation during seaweed bread baking. *LWT, 215*, Article 117260. https://doi.org/10.1016/j.lwt.2024.117260

Karasek, L., Wenzl, T., & Anklam, E. (2009). Determination of acrylamide in roasted chestnuts and chestnut-based foods by isotope dilution HPLC-MS/MS. *Food Chemistry, 114*(4), 1555–1558. https://doi.org/10.1016/j.foodchem.2008.11.057

Keramat, J., Lebail, A., & Prost, C. (2011). Acrylamide in baking products : A review article. *Food and Bioprocess Technology, 4*, 530–543. https://doi.org/10.1007/s11947-010-0495-1

Li, Shichao, Zanchin, Alessandro, Marinello, Francesco, & Guerrini, Lorenzo (2026). Three-dimensional analysis of fruit and vegetables: Sensors and methods. *Computers and Electronics in Agriculture, 245*, 111497. https://doi.org/10.1016/j.compag.2026.111497, 111497 https://linkinghub.elsevier.com/retrieve/pii/S016816992600092X.

Ma, J., Sun, D.-W., Pu, H., Cheng, J.-H., & Wei, Q. (2019). Advanced techniques for hyperspectral imaging in the food industry: Principles and recent applications. *Annual Review of Food Science and Technology, 10*, 197–220. https://doi.org/10.1146/annurev-food-032818-121155. Volume 10, 2019.

Malegori, C., Muncan, J., Mustorgi, E., Tsenkova, R., & Oliveri, P. (2022). Analysing the water spectral pattern by near-infrared spectroscopy and chemometrics as a dynamic multidimensional biomarker in preservation: Rice germ storage monitoring. *Spectrochimica Acta Part A: Molecular and Biomolecular Spectroscopy, 265*, Article 120396. https://doi.org/10.1016/j.saa.2021.120396

Manley, D., & Clark, H. (2011). 39 - Biscuit baking. In D. Manley (Ed.), *Manley's technology of biscuits, crackers and cookies* (4th ed.). Woodhead Publishing. https://doi.org/10.1533/9780857093646.4.477. Fourth Edi, pp. 477–500.

Mesias, M., & Morales, F. J. (2025). Acrylamide- and hydroxymethylfurfural-forming capacity of alternative flours. In *Heated dough systems*.

Mesías, M., Morales, F. J., & Delgado-Andrade, C. (2019). Acrylamide in biscuits commercialised in Spain: A view of the Spanish market from 2007 to 2019. *Food & Function, 10*(10), 6624–6632. https://doi.org/10.1039/c9fo01554j

Mesias, M., & Morales, J. F. (2016). Chapter 7 - Acrylamide in bakery products. In V. Gökmen (Ed.), *Acrylamide in food* (pp. 131–157). Elsevier. https://doi.org/10.1016/B978-0-12-802832-2.00007-3.

Mioara, N., & Culetu, A. (2016). Application of an accurate and validated method for identification and quantification of acrylamide in bread, biscuits and other bakery products using GC-MS/MS system. *Journal of the Brazilian Chemical Society*. https://doi.org/10.5935/0103-5053.20160059

Mollakhalili, N., Khorshidian, N., Nematollahi, A., & Arab, M. (2021). Acrylamide in bread: A review on formation, health risk assessment, and determination by analytical techniques. *Environmental Science and Pollution Research, 28*, 1–19. https://doi.org/10.1007/s11356-021-12775-3

Murkovic, M., & Derler, K. (2006). Analysis of amino acids and carbohydrates in green coffee. *Journal of Biochemical and Biophysical Methods, 69*(1), 25–32. https://doi.org/10.1016/j.jbbm.2006.02.001

Musa, S., Becker, L., Oellig, C., & Scherf, K. A. (2024). Influence of asparaginase on acrylamide content, color, and texture in oat, corn, and rice cookies. *Journal of Agricultural and Food Chemistry, 72*(41), 22875–22882. https://doi.org/10.1021/acs.jafc.4c06175

Muttucumaru, N., Powers, S. J., Elmore, J. S., Mottram, D. S., & Halford, N. G. (2015). Effects of water availability on free amino acids, sugars, and acrylamide-forming potential in potato. *Journal of Agricultural and Food Chemistry, 63*(9), 2566–2575. https://doi.org/10.1021/jf506031w

Safari, A., Salamat, R., & Baik, O.-D. (2018). A review on heat and mass transfer coefficients during deep-fat frying: Determination methods and influencing factors. *Journal of Food Engineering, 230*, 114–123. https://doi.org/10.1016/j.jfoodeng.2018.01.022

Sepehr, A., Carraro, A., Napoli, M., Pescatore, A., & Guerrini, L. (2026). Non-destructive acrylamide quantification in whole-grain bread using RGB-thermal images. *European Food Research and Technology, 252*(2), 73. https://doi.org/10.1007/s00217-025-04972-y

Soni, A., Dixit, Y., Reis, M. M., & Brightwell, G. (2022). Hyperspectral imaging and machine learning in food microbiology: Developments and challenges in detection of bacterial, fungal, and viral contaminants. *Comprehensive Reviews in Food Science and Food Safety, 21*(4), 3717–3745. https://doi.org/10.1111/1541-4337.12983

Takacs, Ronny, Jovicic, Vojislav, Zbogar-Rasic, Ana, Geier, Dominik, Delgado, Antonio, & Becker, Thomas (2020). Evaluation of baking performance by means of mid-infrared imaging. *Innovative Food Science & Emerging Technologies, 61*, 102327. https://doi.org/10.1016/j.ifset.2020.102327, 102327 https://linkinghub.elsevier.com/retrieve/pii/S1466856420302733.

Van Der Fels-Klerx, H. J., Capuano, E., Nguyen, H. T., Ataç Mogol, B., Kocadağlı, T., Göncüoğlu Taş, N., Hamzalıoğlu, A., Van Boekel, M. A. J. S., & Gökmen, V. (2014). Acrylamide and 5-hydroxymethylfurfural formation during baking of biscuits: NaCl and temperature–time profile effects and kinetics. *Food Research International, 57*, 210–217. https://doi.org/10.1016/j.foodres.2014.01.039

Verma, V., & Yadav, N. (2022). Acrylamide content in starch based commercial foods by using high performance liquid chromatography and its association with browning index. *Current Research in Food Science, 5*, 464–470. https://doi.org/10.1016/j.crfs.2022.01.010

Xie, C., Tang, W., Wang, C., Zhang, Y., & Zhao, M. (2024). Hyperspectral imaging for predicting and visualizing the acrylamide levels in roasted coffee. *Microchemical Journal, 202*(January), Article 110685. https://doi.org/10.1016/j.microc.2024.110685

Xie, C., Wang, C., Zhao, M., & Zhao, L. (2023). Prediction of acrylamide content in potato chips using near-infrared spectroscopy. *Spectrochimica Acta, Part A: Molecular and Biomolecular Spectroscopy, 301*(June), Article 122982. https://doi.org/10.1016/j.saa.2023.122982

Yıldız, H. G., Palazoğlu, T. K., Miran, W., Kocadağlı, T., & Gökmen, V. (2017). Evolution of surface temperature and its relationship with acrylamide formation during conventional and vacuum-combined baking of cookies. *Journal of Food Engineering, 197*, 17–23. https://doi.org/10.1016/j.jfoodeng.2016.11.001

Zhang, J., Guo, Z., Ren, Z., Wang, S., Yin, X., Zhang, D., Wang, C., Zheng, H., Du, J., & Ma, C. (2023). A non-destructive determination of protein content in potato flour noodles using near-infrared hyperspectral imaging technology. *Infrared Physics & Technology, 130*, Article 104595. https://doi.org/10.1016/j.infrared.2023.104595

Žilić, S., Dodig, D., Basić, Z., Vančetović, J., Titan, P., Đurić, N., & Tolimir, N. (2017). Free asparagine and sugars profile of cereal species: The potential of cereals for acrylamide formation in foods. *Food Additives \& Contaminants: Part A, 34*(5), 705–713. https://doi.org/10.1080/19440049.2017.1290281